# *Patterns and statistics of in-water polarization under conditions of linear and nonlinear ocean surface waves*



**Citation:** Xu, Zao, Dick K. P. Yue, Lian Shen, and Kenneth J. Voss. "Patterns and Statistics of in-Water Polarization Under Conditions of Linear and Nonlinear Ocean Surface Waves." Journal of Geophysical Research 116, no. C12 (December 6, 2011).

**As Published:** http://dx.doi.org/10.1029/2011JC007350

**Publisher:** American Geophysical Union (AGU)

**Persistent URL:** http://hdl.handle.net/1721.1/120315

**Version:** Final published version: final published article, as it appeared in a journal, conference proceedings, or other formally published context

# Patterns and statistics of in-water polarization under conditions of linear and nonlinear ocean surface waves

Zao Xu,[1] Dick K. P. Yue,[1] Lian Shen,[2] and Kenneth J. Voss[3]

Received 1 June 2011; revised 14 September 2011; accepted 16 September 2011; published 6 December 2011.

[1] We study the polarization properties of the light field under a dynamic ocean surface using realistic linear and nonlinear ocean surface waves. The three-dimensional polarized radiative transfer of the dynamic ocean–atmosphere system is considered using a Monte Carlo vector radiative transfer simulation for arbitrary depth. The program is validated with measurement data taken in Hawaii during the Radiance in a Dynamic Ocean project. The main focus of this study is the influence of the wind-driven ocean waves on the polarization patterns and statistics at different optical depths under various conditions of light wavelength and solar incidence. Of special interest is the effect of the nonlinearity of the surface waves on the polarization statistics. To facilitate the study, phase-resolved direct simulations of the linear and nonlinear surface wavefields are performed using a high-order spectral method. The results show that the time-averaged degree of polarization within the Snell's window is dependent on the mean square slope of the ocean surface. Higher mean square slope, or wind speed, leads to a smaller degree of polarization. At the same time, the variability of the degree of polarization has a strong dependence on the surface roughness. A rougher ocean surface induces higher variability of the degree of polarization. The effect of wave nonlinearity can be neglected for the mean value of polarization, but is manifested in the variability of the degree of polarization, with a general increase in the variance with increasing wave nonlinearity. The present findings provide possible mechanisms for characterizing the dynamic ocean surface based on underwater polarized light measurements.

**Citation:** Xu, Z., D. K. P. Yue, L. Shen, and K. J. Voss (2011), Patterns and statistics of in-water polarization under conditions of linear and nonlinear ocean surface waves, *J. Geophys. Res.*, *116*, C00H12, doi:10.1029/2011JC007350.

## 1. Introduction

[2] The polarization of underwater light has drawn the attention of oceanographers for decades because it contains rich information on ocean constituents, solar condition, and dynamic ocean surface wavefields. Some properties of the polarization have been found to be used for orientation by many marine animals [*Wehner*, 2001]. Pioneering work was done by *Waterman and Westell* [1956] and *Ivanoff and Waterman* [1958] to experimentally investigate the polarized light field distribution in water and its dependence on solar direction, detector depth, water turbidity, and light wavelength. They found that the degree of polarization decreases with increasing depth and in water with higher turbidity. Their quantitative studies indicated that the maximum degree of polarization appeared in scattering angles 90° to the Sun and the minimum degree of polarization in directions toward or away from the Sun.

[3] An important aspect of the study of oceanic polarization is the measurement of the Mueller matrix. *Beardsley* [1968], *Kadyshevich et al.* [1971], and *Voss and Fry* [1984] separately reported measurements of the Mueller matrix for ocean water. Recently, *Liu and Voss* [1997] and *Voss et al.* [2008] reported using fisheye imaging polarimeters to measure the Stokes vector components of the sky and the underwater polarization patterns with high angular resolution. *Sabbah and Shashar* [2006] considered hyperspectral measurements and started a preliminary investigation of the fluctuation of polarization fields induced by ocean surface waves. They found that the variability of the degree of polarization was higher than that of radiance and decreased with depth. *Sabbah and Shashar* [2007] later investigated the special case of in-water light polarization with the Sun near the horizon. They claimed that the underwater polarization at large solar zenith angles cannot be predicted by simple Rayleigh scattering, likely due to the high contribution of skylight.

[4] Besides the experimental work, a considerable amount of theoretical work has been done to understand polarized light propagation in the atmosphere and ocean. *Chandrasekhar* [1950] applied the Stokes vector, which represents the complete polarization state of light, to the

[1]Department of Mechanical Engineering, Massachusetts Institute of Technology, Cambridge, Massachusetts, USA.
[2]Department of Civil Engineering, Johns Hopkins University, Baltimore, Maryland, USA.
[3]Atmospheric and Oceanic Optics Laboratory, Department of Physics, University of Miami, Coral Gables, Florida, USA.


0148-0227/11/2011JC007350

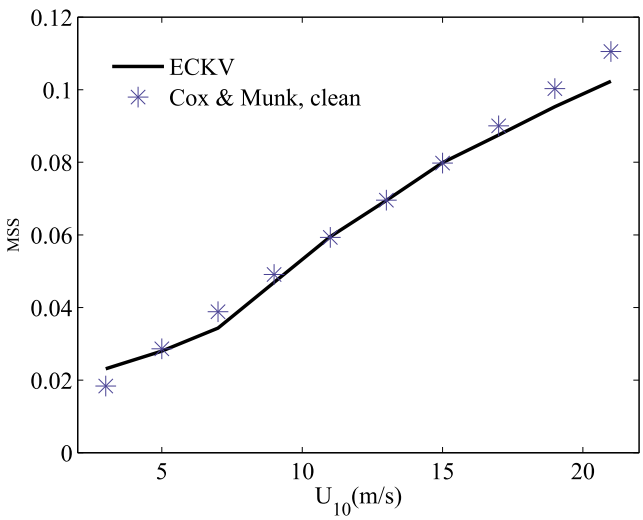


**Figure 1.** MSS dependence on wind speed $U_{10}$ for the ECKV model and Cox-Munk model (clean surface). ECKV model is able to reproduce the MSS measured by Cox-Munk.

classic radiative transfer equation and derived the exact solution of the vector radiative transfer equation (VRTE) for a plane-parallel atmosphere with Rayleigh scattering. *Kattawar and Adams* [1989] introduced a Monte Carlo (MC) method in simulating the polarized light radiative transfer process and provided expressions for the transmission and reflection Muller matrices at a dielectric interface. Rapid development in computing power has made the MC method the most prevalent tool in simulating the polarized light fields in the atmosphere–ocean system.

[5] Previous modeling of the underwater polarized light field was mainly focused on the relations between polarization and water turbidity, solar incidence, and light wavelength. Very few considered the effect of dynamic ocean surfaces because it was thought to be relatively small compared with the effects of solar incidence and ocean turbidity. Also, the lack of a reliable ocean surface model and the difficulty in obtaining realistic, phase-resolved wavefields caused problems. With the assumption of a flat ocean surface, *Horváth and Varjú* [1997] and *Sabbah et al.* [2006] theoretically studied the polarization patterns affected by the air-sea interface. They demonstrated that the in-water polarization is modified through refraction of skylight; the polarization pattern resembles the sky polarization pattern within the Snell's window but with slightly different values. In the previous work studying wave effects on the in-water light fields [*Kattawar et al.*, 1973], the Cox-Munk [*Cox and Munk*, 1954] ocean surface model was used. To represent the realistic ocean, however, there exists a critical need for a phase-resolved wavefield model accounting for all wave modes and wave nonlinearity.

[6] In this study, we first describe the numerical and experimental methods in section 2. We focus on the numerical models including the phase-resolved linear and nonlinear wavefield models and a parallelized three-dimensional MC model to simulate the polarized light radiative transfer in the atmosphere–ocean system. In section 3, we validate the MC model with field measurements. With the above numerical model, we qualitatively and quantitatively investigate the patterns and statistical properties of the underwater polarized light fields induced by the dynamic ocean surface, for example, under different surface wind conditions. We find that the ocean surface with a high mean square slope (MSS) leads to a small degree of polarization and large variability in underwater polarization. Finally, we find that nonlinear ocean waves cause somewhat higher variability of underwater polarization when compared with linear ocean waves.

## 2. Methods and Measurements

### 2.1. Wind-Driven Ocean Wave Model

[7] The spectral model of wind-driven ocean waves we chose is the Elfouhaily, Chapron, Katsaros and Vandemark (ECKV) [*Elfouhaily et al.*, 1997] model, which has been frequently used recently for remote sensing studies. It considers both high-frequency and low-frequency waves. Compared with full wave number models such as those developed by *Donelan and Pierson* [1987], *Bjerkaas and Riedel* [1979], and *Apel* [1994], the ECKV model is capable of reproducing results in agreement with the Cox-Munk observations in the high-frequency region. The omnidirectional spectrum is written as the sum of two spectral regimes combined with a spreading function; the expression of the unified spectrum is

$$S(k,\varphi) = \frac{1}{2\pi}k^{-4}[B_l + B_h][1 + \Delta(k)\cos(2\varphi)], \qquad (1)$$

where $B_l$ and $B_h$ indicate the curvature spectra of the low-frequency and high-frequency parts, respectively. The ratio parameter $\Delta(k)$ can be regarded as the coefficient of the second harmonic of the Fourier series expansion of the spreading function. The exact solutions of $B_l$, $B_h$, and $\Delta(k)$ are given by *Elfouhaily et al.* [1997]. Figure 1 shows a comparison of the MSS between the Cox-Munk model and the ECKV model.

[8] Most studies in remote sensing use linear wave realizations based on various wave spectral models. As such, the ocean surface is regarded as an incoherent summation of independently evolving wave modes. This assumption leads to a Gaussian distribution for the surface slopes and curvatures. However, it has been shown in both experiments and simulations that at later stages of ocean wavefield evolution, nonlinearity plays a major role in the wave evolution and the energy exchange among different wave modes. Therefore, the Gaussian assumption is invalid for a fully developed sea. To obtain more realistic dynamic ocean surfaces, we use a high-order spectral (HOS) method to simulate the dynamic evolution of wavefields starting from a JONSWAP [*Hasselmann et al.*, 1973] spectrum. The HOS method was developed independently by *Dommermuth and Yue* [1987] and *West et al.* [1987] and has been serving as a powerful numerical tool for the simulation of nonlinear waves. This method combines the ideas of mode coupling and order expansion. It accounts for nonlinear interactions up to an arbitrary order of perturbations in wave steepness, and it can simulate a large number (for example, $O(10^3)$) of free wave modes per horizontal dimension. With the fast Fourier transform technique, the computation effort is almost linearly proportional to the total number of modes and the order of

nonlinearity, which makes the HOS method a highly efficient and accurate numerical method to solve wave problems such as long-term nonlinear wave interaction and evolution. In this study, we use HOS simulations to obtain nonlinear phase-resolved ocean surface wavefields.

### 2.2. Parallel MC Solution of VRTE

[9] The VRTE that describes the propagation of the Stokes vector is written as

$$\Omega \cdot \nabla \mathbf{I}(\Omega, \mathbf{x}) + c\mathbf{I}(\Omega, \mathbf{x}) = \frac{b}{4\pi}\int_{4\pi} \mathbf{P}(\Omega', \Omega)\mathbf{I}(\Omega', \mathbf{x})d\Omega', \qquad (2)$$

where $\mathbf{I}$ is the Stokes vector with four components $\mathbf{I} = [I, Q, U, V]^T$, which have the units of light intensity per unit area per solid angle, W m$^{-2}$ sr$^{-1}$. All information about the polarized light is contained in these four components. $\Omega$ is the solid angle which represents the direction of the polarized light. The relation between solid angle $\Omega$ and direction in polar coordinates ($\theta$, $\phi$) can be expressed as $d\Omega = \sin\theta d\theta d\phi$; $c$ and $b$ are the beam attenuation coefficient and beam scattering coefficients, respectively. The single scattering albedo $\omega$ is defined as $\omega = b/c$. The phase matrix $\mathbf{P}(\Omega', \Omega)$ inside of the integral in equation (2) accounts for the transformation of the incident Stokes vector $\mathbf{I}_{inc}$ with direction $\Omega'$ to the scattered Stokes vector $\mathbf{I}_{sca}$ with direction $\Omega$. $\mathbf{P}(\Omega', \Omega)$ can be expressed as

$$\mathbf{P}(\Omega', \Omega) = \mathbf{R}(-\Phi)\mathbf{M}(\Theta_{sca})\mathbf{R}(-\Psi_{sca}), \qquad (3)$$

where $\Theta_{sca}$ and $\Psi_{sca}$ are the scattering polar and rotation angle, respectively. Their relation to the incident direction $\Omega'$ and the scattered direction $\Omega$ is demonstrated in Figure 2; $\mathbf{R}(\psi)$ is the rotation matrix denoting the transformation of the Stokes vector when rotating the reference coordinate by $\psi$; and $\mathbf{M}$ is a $4 \times 4$ scattering Mueller matrix that describes the scattering process relative to the scattering plane. Instead of using the Rayleigh scattering Mueller matrix [*Kattawar and Adams*, 1989], *Chandrasekhar and Elbert* [1954] expressed the reduced Mueller matrix to account for the anisotropy in the polarizability tensor as

$$\mathbf{M} = \frac{1+\mu^2}{2} \times \begin{pmatrix} 1 & \frac{(1-\rho)(\mu^2-1)}{(1+\mu^2)+(3-\mu^2)\rho} & 0 & 0 \\ \frac{(1-\rho)(\mu^2-1)}{(1+\mu^2)+(3-\mu^2)\rho} & \frac{(1-\rho)(\mu^2+1)}{(1+\mu^2)+(3-\mu^2)\rho} & 0 & 0 \\ 0 & 0 & \frac{(2-2\rho)\mu}{(1+\mu^2)+(3-\mu^2)\rho} & 0 \\ 0 & 0 & 0 & \frac{(2-6\rho)\mu}{(1+\mu^2)+(3-\mu^2)\rho} \end{pmatrix}, \qquad (4)$$

where $\mu = \cos\Theta_{sca}$; and $\rho$ is the depolarization ratio with the commonly used values for the atmosphere and ocean being $\rho_{atm} = 0.0279$ and $\rho_{ocn} = 0.09$, respectively, under the clear sky condition.

[10] The three-dimensional polarized light radiative transfer process is simulated with the MC method in order to calculate all orders of scattering. Several biased sampling techniques are employed in choosing photon traveling path length, source function, and scattering angle to reduce the variance of the results and account for the Mie scattering. The technique of introducing the Mie scattering phase function to the Rayleigh Mueller matrix was developed by *Tynes et al.* [2001]. The scattering polar and azimuthal angle ($\Theta_{sca}$, $\Psi_{sca}$) can be obtained by first selecting $\Theta_{sca}$ from the phase function for unpolarized light $p(\Theta_{sca})$ and then sampling the conditional probability density function for $\Psi_{sca}$ given $\Theta_{sca}$

$$p(\Psi_{sca}|\Theta_{sca}) = \frac{1}{p_{\max}(\Psi_{sca}|\Theta_{sca})} \times \left[I + \frac{\mu^2-1}{\mu^2+1}(Q\cos 2\Psi_{sca} + U\sin 2\Psi_{sca})\right], \qquad (5)$$

where

$$p_{\max}(\Psi_{sca}|\Theta_{sca}) = I + \frac{1-\mu^2}{1+\mu^2}\sqrt{Q^2+U^2}. \qquad (6)$$

[11] At the air-sea interface, we used the refraction Mueller matrix and reflection Mueller matrix introduced by *Kattawar*

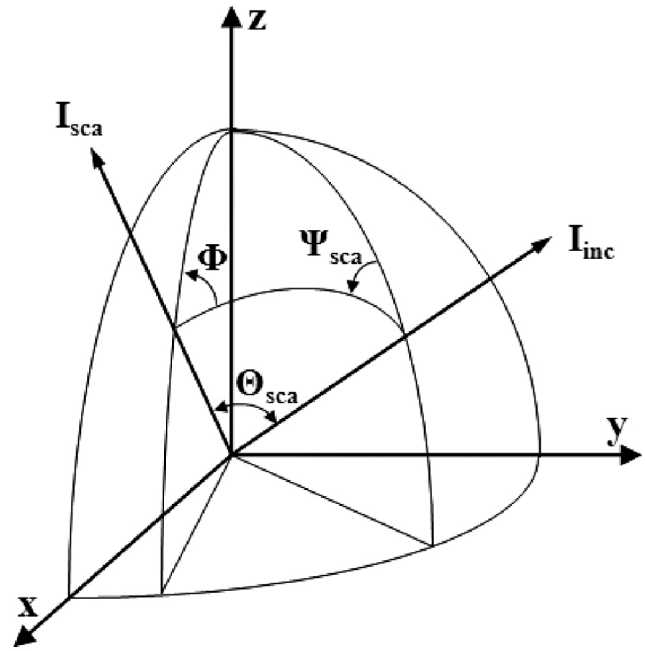


**Figure 2.** Geometry of rotations for Stokes vector transformation. The directions of the polarized light before scattering $\mathbf{I}_{inc}$ and after scattering $\mathbf{I}_{sca}$ are $\mathbf{\Omega}'$ and $\mathbf{\Omega}$, respectively. $\Theta_{sca}$ and $\Psi_{sca}$ are the two rotated angles in equation (3).

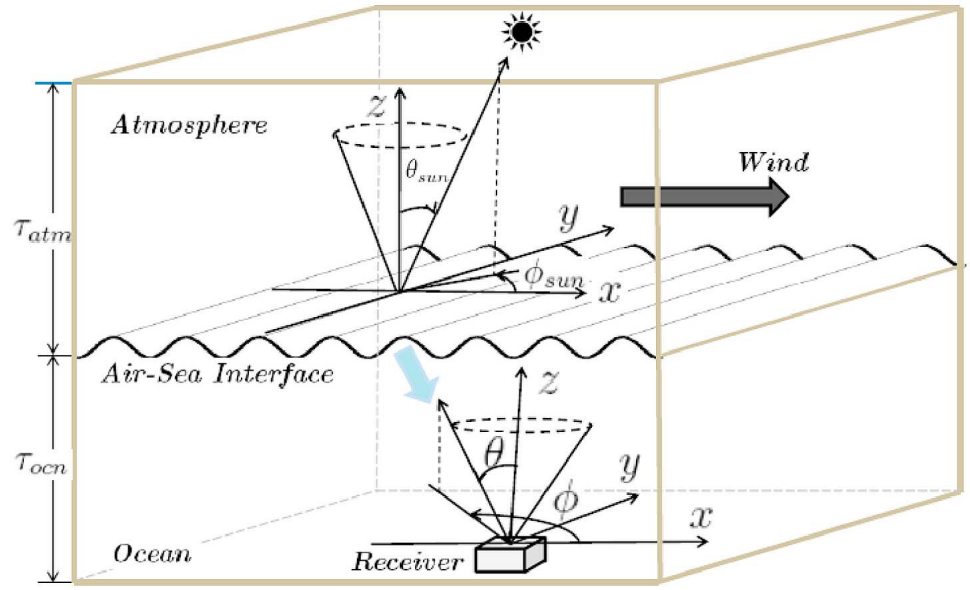


**Figure 3.** Sketch of the atmosphere–ocean system. Here $\theta_{sun}$ and $\phi_{sun}$ are the solar zenith angle and azimuth angle, respectively; ($\theta$, $\phi$) is the central direction of the bin of photons detected by the receiver. The upwind direction is along the positive $\hat{\mathbf{x}}$ axis.

*and Adams* [1989] to account for refraction and reflection, including total internal reflection.

[12] We validate the MC program by making model-to-model comparisons with results of *Tynes et al.* [2001]. Model-to-data validation will be given below in comparison with the Hawaii experiment of the Radiance in a Dynamic Ocean (RaDyO) project [*Dickey et al.*, 2011].

[13] Even with the variance reducing techniques, the MC simulation is still computationally expensive. Therefore, a full parallelization of the MC program is completed using Message Passing Interface. The parallelized programme has been executed on the supercomputers of the U.S. Department of Defence High-Performance Computing system using up to $10^3$ processors.

### 2.3. Atmosphere–Ocean System

[14] The atmosphere–ocean system considered in our simulations is illustrated in Figure 3. As shown, $\theta_{sun}$ and $\phi_{sun}$ are the solar zenith angle and azimuth angle, respectively; ($\theta$, $\phi$) is the central direction of the bin of photons detected by the receiver. The downwind direction is along the positive $\hat{\mathbf{x}}$ axis. A plane-parallel geometry is assumed with multilayers for both the atmosphere and ocean. Based on the Maritime Aerosol Model I (MAR-I) [*Adams and Gray*, 2011], the atmosphere is treated as a two-layer system. The upper layer contains continental-type aerosols, and the lower layer contains maritime-type aerosols. Assume $\tau_m$ is the optical thickness of the maritime haze layer, $\tau_c$ is the optical thickness of the continental haze layer, and $\tau_r$ is the optical thickness of the Rayleigh scattering layer. We have

$$\tau_c = 0.025, \tau_r = 0.114, \omega = 0.957. \tag{7}$$

For the bottom layer,

$$\tau_m = 0.05, \tau_r = 0.031, \omega = 1. \tag{8}$$

[15] We assume that the ocean layer is a homogeneous water body with three components which are pure water (subscript $w$), suspended particles (subscript $p$), and colored dissolved organic matter (CDOM) (subscript $g$). The ocean inherent optical properties (IOPs) include the beam attenuation coefficient of pure water $c_w$, the single scattering albedo of pure water $\omega_w$ [*Smith and Baker*, 1981; *Pope and Fry*, 1997], the particulate and CDOM beam attenuation coefficient $c_{pg}$, and the single scattering albedo of particles and CDOM $\omega_{pg}$. The ocean IOPs of particles and CDOM, used in the simulations listed in Tables 1 and 2, were obtained from the RaDyO experiments in Hawaii in September 2009 and in Santa Barbara Channel (SBC) in September 2008 [*Dickey et al.*, 2011], respectively. The volume scattering functions for both atmospheric layers are approximated as the Rayleigh scattering phase function. The volume scattering

**Table 1.** Ocean IOPs of the Hawaii Experiment Used in the Simulations

| $\lambda$ (nm) | $c_w$ ($m^{-1}$) | $\omega_w$ | $c_{pg}$ ($m^{-1}$) | $\omega_{pg}$ |
|---|---|---|---|---|
| 520 | 0.043 | 0.0422 | 0.097 | 0.546 |
| 550 | 0.058 | 0.026 | 0.111 | 0.469 |

**Table 2.** Ocean IOPs of the SBC Experiment Used in the Simulations

| $\lambda$ (nm) | $c_w$ ($m^{-1}$) | $\omega_w$ | $c_{pg}$ ($m^{-1}$) | $\omega_{pg}$ |
|---|---|---|---|---|
| 443 | 0.011 | 0.394 | 0.785 | 0.848 |
| 532 | 0.046 | 0.046 | 0.652 | 0.931 |
| 670 | 0.440 | 0.002 | 0.487 | 0.918 |

function for the ocean used in the simulation is the Petzold phase function [*Petzold*, 1972].

[16] It is worth mentioning that in this study, since the sky polarization is considered only as an input, several approximations are made for atmospheric layers for simplicity: the dependence of atmosphere optical thickness on light wavelength is ignored. In addition, the high anisotropy of the aerosol phase function is neglected and it is approximated with the Rayleigh scattering phase function due to the fact that the aerosol optical thickness is very small. This approximation could possibly lead to a slight underestimation in the underwater polarization. Here for simplicity we assume that the neglected small angle scattering does not change radiance/polarization distribution significantly.

### 2.4. Field Measurements

[17] Measurement of the polarized light field were made during the RaDyO SBC experiment in September 2008 and Hawaii experiment in September 2009. The downwelling sky polarized radiance distribution was obtained with the Skycam system, which is a fisheye imaging polarimeter in a stabilized mount, similar to *Liu and Voss* [1997] and *Voss and Liu* [1997]. This system takes 3 sequential images, with linear polarizers in different orientations, to obtain 3 of the 4 Stokes parameters ($I$, $Q$, and $U$). An important quantity, the degree of linear polarization (DOLP), can be defined via $I$, $Q$, and $U$ to measure the proportion of linearly polarized light

$$DOLP = \frac{\sqrt{Q^2 + U^2}}{I}. \tag{9}$$

The in-water measurements were taken with the downwelling polarized radiance distribution camera system (DPOL) system [*Bhandari et al.*, 2011b]. This system has four fisheye lenses, and takes the four images required for calculating the Stokes vector simultaneously. (More data on these systems is available from *Bhandari et al.* [2011a].) For the data shown in this paper, the DOLP was abstracted along the principal plane, and 5–10 images were averaged. As can be seen in the work of *Bhandari et al.* [2011a], around the zenith direction there are a lot of artifacts because of the support cable and support booms. These cause the retrieved minimum P to be in error and much larger than it should be.

[18] The uncertainty of the sky polarization measurements is estimated to be 0.05 for $Q/I$, $U/I$ and the DOLP. For the in-water measurements the uncertainty in Q/I and U/I is approximately 0.06, while for the DOLP the uncertainty is 0.05 when the DOLP is > 0.10. For values of the DOLP < 0.10, there is a positive bias which increases as the DOLP goes to zero, and results in a minimum DOLP of 0.05 for unpolarized light.

## 3. Results

### 3.1. Skylight Polarization

[19] The downwelling polarization pattern at the surface is critical in understanding the in-water polarization [*Horváth and Varjú*, 1997]. With the atmosphere configuration described earlier, we can obtain the Stokes vector for the sky polarization just above the ocean surface. The polarization properties such as the degree of polarization $P$ and $e$ vector $\chi$ can be quantified according to their definitions

$$P = \frac{\sqrt{Q^2 + U^2 + V^2}}{I}, \tag{10}$$

$$\tan(2\chi) = \frac{U}{Q}. \tag{11}$$

Here $P$ indicates the proportion of light that is polarized; and the orientation of $\chi$ represents the dominant vibration plane of the electromagnetic wave.

[20] The sky polarization obtained by the MC simulation is compared with the field data collected during the RaDyO experiment in Hawaii. Comparison is performed for quantities including $P$, $\chi$, $U/I$, and $Q/I$, as shown in Figure 4. The experiments were performed under the condition that the solar zenith was at the position of ($\theta_{sun} \approx 65°$, $\phi_{sun} = 0°$) and the sky was clear. We can see that the simulated skylight polarization is in good agreement with the experimental data. Specifically, we evaluate the degree of fit between modeled and measured data with the correlation coefficient $r$ for all four quantities. The analysis shows that the correlation coefficient $r$ for $P$, $\chi$, $U/I$, and $Q/I$ are $r_P = 0.943$, $r_\chi = 0.935$, $r_{U/I} = 0.954$, and $r_{Q/I} = 0.966$, respectively. Therefore, the modeled sky polarization can be used as a reliable input for the investigation of underwater polarization.

### 3.2. In-Water Polarization

[21] It is known that light in water is only partially linearly polarized, except at very shallow depths where total internal reflection can cause a nonzero Stokes component $V$ [*Ivanoff and Waterman*, 1958]. Measurements of the DOLP were taken on 5 September 2009 in Hawaii. The measurement conditions are listed in Table 3. The sky was clear most of the day. Wind speed was in the range from 6.1 to 8.2 m s$^{-1}$. Three measurement depths were chosen: 1 m and 2 m at 520 nm and 8 m at 550 nm. We evaluated the DOLP distribution in the principal plane. Five instantaneous DOLP measurements were averaged to reduce the noise.

[22] Figure 5 shows comparisons of the measurement data and the MC model results. Receiver size has been tested using 5 cm and 2 cm. Only slight differences are found and therefore the receiver size used in the simulation is 2 cm. The angular bin size chosen is ($\Delta\theta$, $\Delta\phi$) = (2°, 2°). IOPs used in the simulation are listed in Table 1. Specifically, the degree of fit between the modeled and the measured DOLP are evaluated with two quantities: $\Delta$DOLP = |DOLP$_{model}$ − DOLP$_{measure}$| and the correlation coefficient $r$. The four cases have $\theta_{sun} = 11°$ shown in Figure 5a, $\theta_{sun} = 46°$ shown in Figure 5b, $\theta_{sun} = 66°$ shown in Figure 5c, and $\theta_{sun} = 76°$ shown in Figure 5d. For measured polar angles from −90° to 90° for four cases the values of $\Delta$DOLP are 0.120 ± 0.088 (average ± standard deviation), 0.080 ± 0.054, 0.062 ± 0.053, and 0.077 ± 0.059 and the correlation coefficient, $r$, was 0.832, 0.813, 0.744, and 0.628. When considering only angles inside the Snell's window (from −48° to 48°), the values of $\Delta$DOLP are 0.056 ± 0.035, 0.064 ± 0.041, 0.041 ± 0.027, and 0.060 ± 0.046; the correlation coefficient, $r$, was 0.943, 0.961, 0.939, and 0.743. It is seen

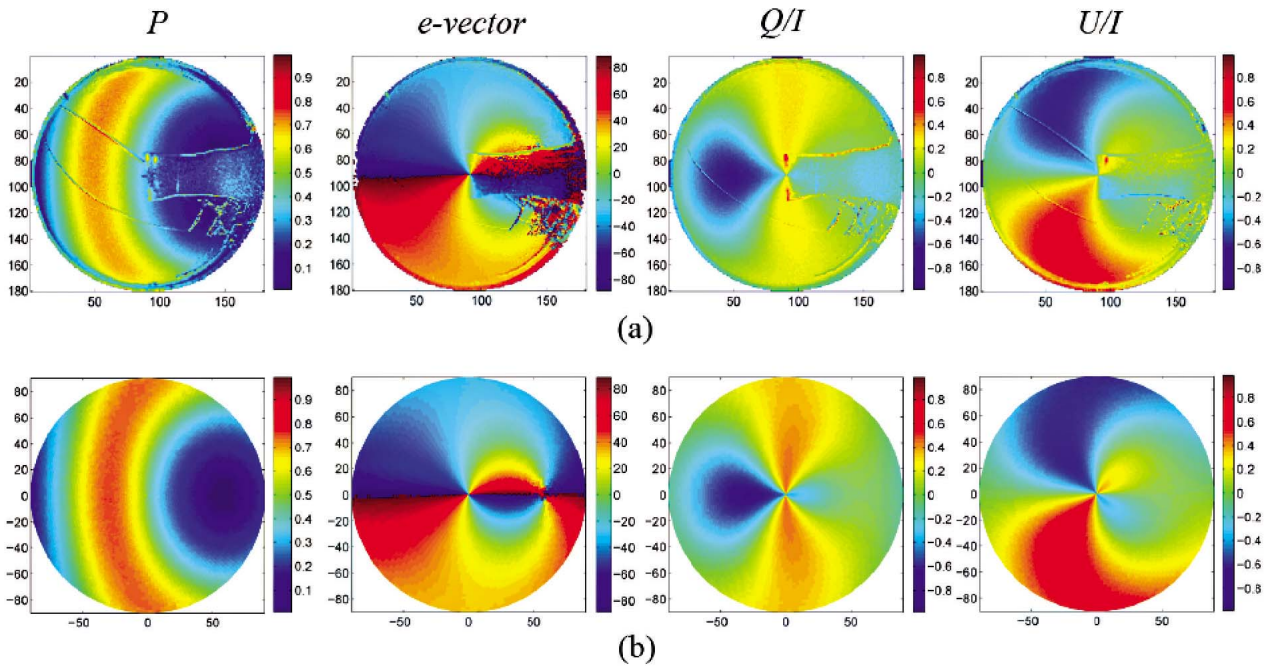


**Figure 4.** Comparison of degree of polarization $P$, $e$ vector $\chi$, and Stokes vector components $Q/I$ and $U/I$ of sky polarization between (a) experimental data collected during the RaDyO experiment in Hawaii and (b) MC simulation results under the condition that solar position was at the direction of ($\theta_{sun} \approx 65°$, $\phi_{sun} = 0°$) and the sky was clear. It is seen that the measured and predicted sky polarization have a very good agreement with each other.

that the value of ΔDOLP inside the Snell's window is significantly smaller than that for all angles in both mean value and standard deviation; the correlation coefficient $r$ inside the Snell's window is 0.1 bigger than that of all angle measurements. Therefore, the comparison between the model and the measurement shows good agreements with each other, especially inside the Snell's window. However, the discrepancy between predictions and measurements occurs mainly at the polar angles outside the Snell's window, particularly for small zenith angles and shallow detector depths. Model predictions are slightly higher than those of measurement at such areas. This is probably because the Mueller matrix for ocean particulates [*Voss and Fry*, 1984] is less polarizing than the matrix used in these simulations. The important Mueller matrix element for polarizing the unpolarized solar beam is the $M_{12}$ matrix element, which at the scattering angle of 90 degrees, was approximately −0.9 versus −0.65 in the Voss and Fry measurements. For high solar zenith angles, this scattering angle is inside the Snell's window on the principle plane, thus the refracted skylight will dominate the shallow water radiance distribution. However, at small solar zenith angles, light on the horizon scattered at 90 degrees can, after a grazing reflection of the ocean surface, be at angles outside the Snell's window in the downwelling field. Using more precise Mueller matrix would improve agreement in these cases. The uncertainty of DOLP for current simulations is around 0.1 outside the Snell's window and it is less than 0.05 inside the Snell's window.

[23] It is known that the maximum DOLP in the air is around 90° to the solar incidence direction due to Rayleigh scattering. In the water, the two maximum DOLPs are located at 90° to the solar incidence direction in water [*Waterman and Westell*, 1956]. Besides the two maximum points caused by oceanic particle scattering, a local maximum DOLP appears inside the Snell's window. This is the transmission of the maximum DOLP in the skylight above the ocean surface.

[24] We defined $\kappa$ as the ratio of the maximum DOLP to the sky degree of polarization $P_{sky}$ to represent the transmission properties of polarization by the rough ocean surface

$$\kappa = \frac{DOLP}{P_{sky}}. \tag{12}$$

Table 4 demonstrates the local maximum DOLP and the ratio $\kappa$ within the Snell's window for both measurement and MC simulation. The two methods agree with each other well. The local maxima of data set 1 to data set 4 are located at ($\theta \approx 45°$, $\phi = 180°$), ($\theta \approx 30°$, $\phi = 180°$), ($\theta \approx 19°$, $\phi = 180°$), and ($\theta \approx 10°$, $\phi = 180°$), respectively. Comparing the data sets 1 to 4, some qualitative features of $\kappa$ can be found. At the same depth, $\kappa$ has a large value in low Sun elevations and a small value for small solar zenith angle.

**Table 3.** Conditions of Data Sets on 5 September 2009 During the Hawaii Experiment

| Data Set | $\lambda$ (nm) | Sky Condition | $U_{10}$ (m s$^{-1}$) | Depth $z$(m) | $\theta_{sun}$ (deg) |
|---|---|---|---|---|---|
| 1 | 520 | Clear | 7.7 | − 1 | 11 |
| 2 | 520 | Clear | 8.2 | − 2 | 46 |
| 3 | 550 | Clear | 6.1 | − 8 | 66 |
| 4 | 520 | Clear | 6.2 | − 1 | 76 |

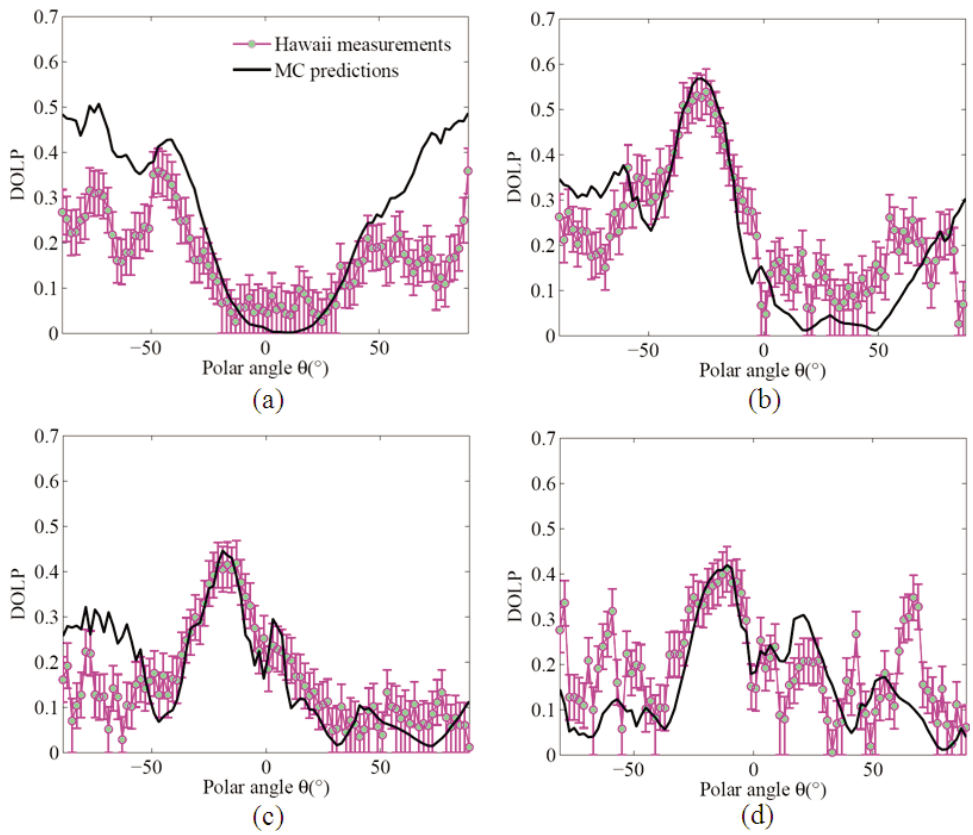


**Figure 5.** Comparison of MC predicted in-water DOLP and measured in-water DOLP in Hawaii in the principal plane for different conditions listed in Table 3. All data were taken with clear sky and with wind speeds ranging from around 6 to 8 m s$^{-1}$. (a) Solar zenith angle $\theta_{sun} = 11°$; receiver placed at $z = -1$ m; light wavelength $\lambda = 520$ nm. (b) Solar zenith angle $\theta_{sun} = 46°$; receiver placed at $z = -2$ m; light wavelength $\lambda = 520$ nm. (c) Solar zenith angle $\theta_{sun} = 66°$; receiver placed at $z = -8$ m; light wavelength $\lambda = 550$ nm. (d) Solar zenith angle $\theta_{sun} = 76°$; receiver placed at $z = -1$ m; light wavelength $\lambda = 520$ nm. The uncertainty of measurements for DOLP is 0.05 when DOLP > 0.1 and the lower bound goes to zero when DOLP < 0.1. Good agreements between MC predictions and measurements are achieved.

The reason is that low Sun elevation puts the maximum DOLP at around zenith, while high Sun elevation puts the maximum DOLP on the horizon, and the corresponding transmitted local maximum DOLP is at the edge of Snell's window. The polarization in the in-water light field within the Snell's window, very near the surface, is determined by the refracted skylight. At large zenith angles, approaching the edge of the Snell's window, small changes in surface slope cause large changes in the portion of the sky responsible for that portion of the subsurface light field. When the maximum DOLP in the sky is near the horizon, waves on the air-sea interface cause the subsurface light field to be a combination of skylight from many different directions, which when added together, decrease the DOLP. When considering the DOLP at the large view zenith angle ($\theta \approx 90°$) and for the case of large solar zenith angle, the results are consistent with the findings of *Sabbah and Shashar* [2007].

#### 3.2.1. Polarization Patterns Affected by Ocean Waves

[25] Our interest is in the ocean surface effects on in-water polarization. *Horváth and Varjú* [1997] studied theoretically the in-water polarization patterns for a flat surface. They demonstrated that the in-water polarization is modified through refraction of skylight; the polarization pattern has resemblance of sky polarization pattern within the Snell's window but with slightly different value. *Sabbah and Shashar* [2006] investigated experimentally the fluctuating features of the effect of dynamic ocean waves on the in-water polarization. They claimed that the variability of degree of polarization was significantly higher than that of the radiance and they demonstrated the viewing direction of the highest light variability in water. To further understand the fluctuations of the underwater polarization, more quantitative analysis is needed.

[26] We began with the instantaneous polarization patterns using the MC simulation. Figure 6 shows qualitatively the

**Table 4.** Maximum DOLP and $\kappa$ for the Hawaii Experiment

| | | DOLP | | $\kappa$ | |
|---|---|---|---|---|---|
| Data Set | $P_{sky}$ | Measurement | MC | Measurement | MC |
| 1 | 0.65 | 0.37 | 0.42 | 0.57 | 0.65 |
| 2 | 0.68 | 0.54 | 0.56 | 0.80 | 0.82 |
| 3 | 0.67 | 0.42 | 0.43 | 0.63 | 0.64 |
| 4 | 0.5 | 0.39 | 0.41 | 0.79 | 0.82 |

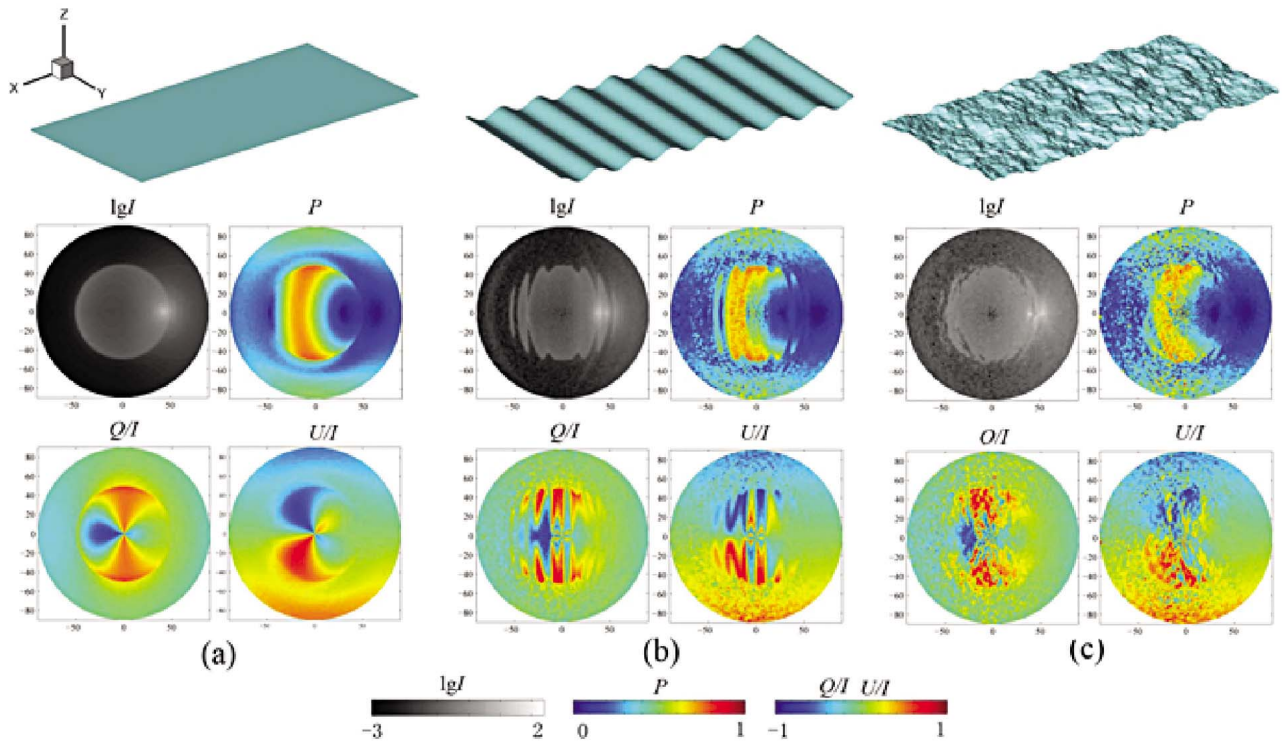


**Figure 6.** Qualitative patterns of stokes vector components $I$, $Q/I$, and $U/I$, and degree of polarization $P$ for three types of ocean surfaces: (a) flat ocean surface, (b) ocean surface with a regular sinusoidal wave, and (c) ocean surface with irregular broadband waves. The solar zenith incidence is ($\theta_{sun}$ = 65°, $\phi_{sun}$ = 0°) and the receiver is placed at the optical depth $\tau = cz = -0.5$.

downwelling polarization patterns for three types of ocean surfaces. The solar incidence for the three cases is ($\theta_{sun}$ = 65°, $\phi$ = 0°). The wavelength of light chosen in the simulation is 532 nm. IOPs are taken from the Hawaii experiments. The upwind direction lies in the principal plane. Receivers are placed at an optical depth $\tau = cz = -0.5$.

[27] We can see that for the flat ocean surface case plotted in Figure 6a, the degree of polarization $P$ and the stokes components $Q/I$ and $U/I$ are similar to the sky polarization pattern, but they are confined within the Snell's window. The maximum degree of polarization is along the contour refracted from 90° to solar incidence in air. Outside the Snell's window, the polarization is due to the scattering of solar light in water. The maximum degree of polarization in water drops slightly after refraction at the interface. For the sinusoidal surface wave case shown in Figure 6b, the polarization quantities show periodicity due to the periodic features of the surface. For the broadband random sea case shown in Figure 6c, the surface consists of waves with different sizes and slopes. Short waves have a strong influence on instantaneous polarization patterns. Although the largest Stokes components are still confined within the Snell's window, ripples can be observed at the edge of the Snell's window in the polarized radiance pattern. The degree of polarization contour line becomes discontinuous within the Snell's window. A high value of the degree of polarization can be seen at the edge of Snell's window, which is due to total internal reflection.

[28] The instantaneous pattern of in-water polarization in the upper ocean is strongly affected by the dynamic sea surface, which leads itself to a statistical treatment.

#### 3.2.2. Time Series of In-Water Polarization

[29] To obtain realistic results in MC simulations, we used the parameters of the receiver comparable to the experimental setup. We chose a receiver size of 5 cm and an angular bin size ($\Delta\theta$, $\Delta\phi$) = (2°, 2°) in all calculations. We selected the solar zenith incidence as ($\theta_{sun}$ = 65°, $\phi_{sun}$ = 0°) in air so that the local maximum degree of polarization is located at ($\theta \approx$ 18°, $\phi$ = 180°) in water.

[30] We obtained 200 realizations of wind-driven surface wave elevations based on the ECKV spectrum and linear boundary conditions to mimic the evolving dynamic ocean surface. The sampling frequency of wave realizations is 10 Hz. Therefore, 20 s of data are recorded for analysis. The minimum wavelength used to generate the wind-driven waves is 4 mm.

[31] A periodic condition is applied to the 9 m × 4.5 m computational domain. We use IOPs measured from the Santa Barbara Channel experiment to understand the influence of relatively high water turbidity on the polarization in the presence of dynamic surface waves. As Table 2 shows, three wavelengths $\lambda$ = 443 nm, 532 nm, and 670 nm are considered. Receivers are placed at depths up to 7.5 m below the surface ($\tau$ = 5 for $\lambda$ = 532 nm). In order to obtain convergent results, the total number of photon launched in each wave surface realization is $4 \times 10^{10}$.

[32] We took the average of the angularly dependent degree of polarization $P(\theta, \phi, t)$ over the 200 realizations and

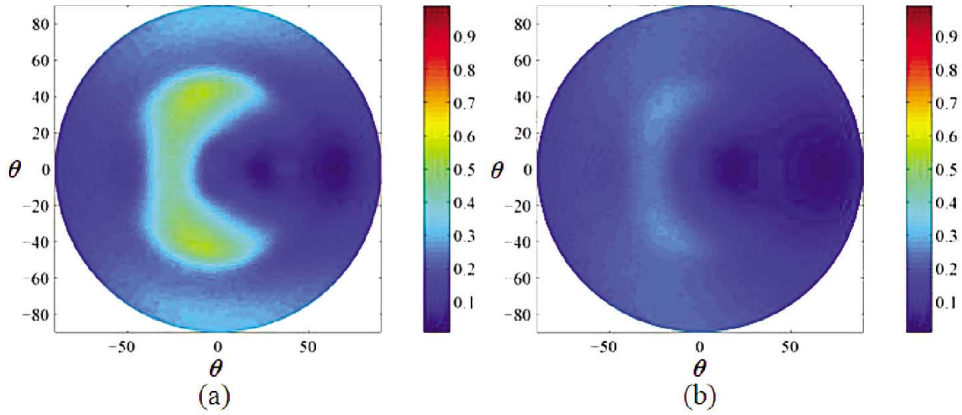


**Figure 7.** Patterns of time-averaged degree of polarization $\langle P \rangle$ at the depths (a) $z = -0.3$ and (b) $z = -3.75$ m. The solar incidence is ($\theta_{sun} = 65°$, $\phi_{sun} = 0°$); the light wavelength $\lambda = 532$ nm; IOPs are obtained from the SBC experiment listed in Table 2. The total beam attenuation coefficient is $c = 0.610$ m$^{-1}$ and total single scattering albedo is $\omega = 0.873$.

obtained the mean value of the in-water degree of polarization. Figures 7a and 7b show $\langle P \rangle$ at a depth next to the surface, $z = -0.3$ m, and at a deeper depth, $z = -3.75$ m, for the case with the wind speed $U_{10} = 11$ m s$^{-1}$. The observation polar angle $\theta$ ranges from 0° to 90°. The mean value $\langle P \rangle$ gives a pattern similar to the flat surface case. At a depth right below the surface, $z = -0.3$ m, $\langle P \rangle$ shows a resemblance to the sky polarization, but is confined inside the Snell's window. Unlike the flat surface case, in which the degree of polarization has uniform value along the transmittal contour 90° to solar incidence in air, the mean value of the degree of polarization has a relatively small value in the principal plane. The maximum value of $\langle P \rangle$ is around 0.6, and is located at two symmetric points ($\theta$, $\phi$) ≈ (40°, ±100°). At the deeper depth (Figure 7b), the maximum value of $\langle P \rangle$ drops to around 0.3. Two other interesting points located on the principal plane are at ($\theta \approx 18°$, $\phi = 0°$) and at ($\theta \approx 60°$, $\phi = 0°$), which are respectively the Babinet point and the Brewster point in the case of flat ocean surface. For flat surface, the two neutral points are the positions of zero linear degree of polarization. However, for the wind-roughened surface, the locations of these two neutral points shift slightly because of the tilted ocean surface and because $\langle P \rangle$ at these two points becomes nonzero.

### 3.2.3. Relation With Wind Speed $U_{10}$

[33] Next, we quantitatively investigate the relation between the in-water polarization fluctuations and the wind speed, $U_{10}$, ranging from 3 to 21 m s$^{-1}$. In Figure 8, the profile of $\langle P \rangle$ on the principal plane at two depths $z = -0.3$ m (Figure 8a) and $z = -4.8$ m (Figure 8b) are given under three different wind speed conditions, $U_{10} = 3$, 11, and 21 m s$^{-1}$. The solar incidence is in the direction of ($\theta_{sun} = 65°$, $\phi_{sun} = 0°$). The wavelength of light is 532 nm, which gives the total beam attenuation coefficient $c = 0.610$ m$^{-1}$ and single scattering albedo $\omega = 0.873$.

[34] The profiles of $\langle P \rangle$ in this turbid water show strong scattering effects of direct incident light in water. As a result,

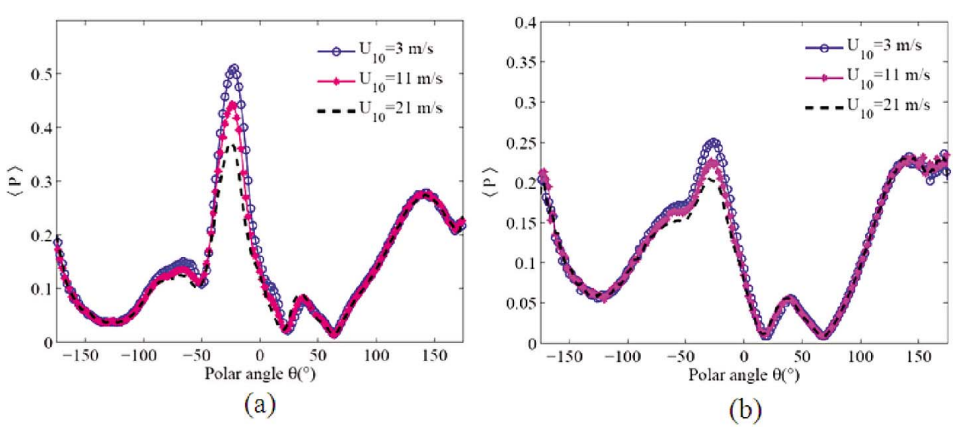


**Figure 8.** Time-averaged degree of polarization $\langle P \rangle$ in the principal plane under different ocean surface conditions ($U_{10} = 3$, 11, and 21 m s$^{-1}$). Receiver placed at the depths (a) $z = -0.3$ and (b) $z = -4.8$ m. The solar incidence is ($\theta_{sun} = 65°$, $\phi_{sun} = 0°$); the light wavelength is $\lambda = 532$ nm; IOPs are obtained from the SBC experiment listed in Table 2. The total beam attenuation coefficient is $c = 0.610$ m$^{-1}$ and total single scattering albedo is $\omega = 0.873$.

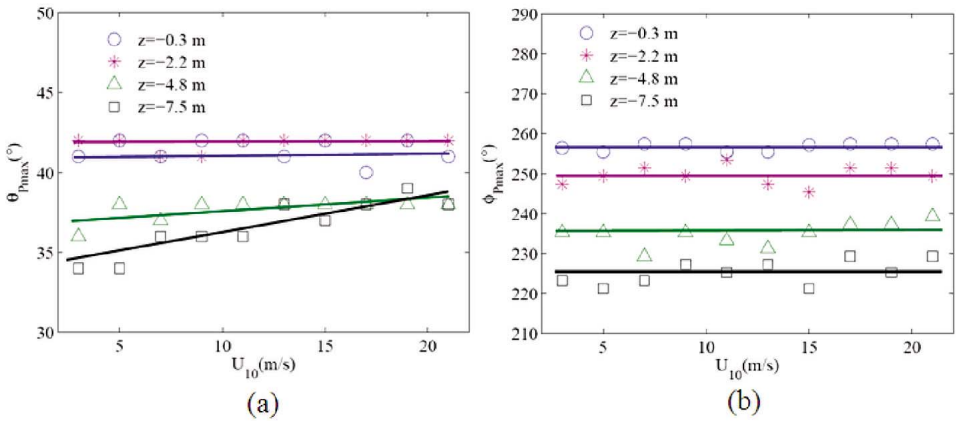


**Figure 9.** Angular position of the maximum mean value of degree of polarization $\langle P\rangle_{\max}$ within the Snell's window at four different depths ($z = -0.3$, $-2.2$, $-4.8$, and $-7.5$ m) under different ocean surface conditions ($U_{10} = 3$, 11, and 21 m s$^{-1}$). (a) Polar angle $\theta_{p_{\max}}$ and (b) azimuth angle $\phi_{p_{\max}}$. The solar incidence is ($\theta_{sun} = 65°$, $\phi_{sun} = 0°$); the light wavelength $\lambda = 532$ nm; IOPs are obtained from the SBC experiment listed in Table 2. The total beam attenuation coefficient is $c = 0.610$ m$^{-1}$ and total single scattering albedo is $\omega = 0.873$.

the light outside the Snell's window becomes partially linearly polarized. The strongest polarization of light appears inside the Snell's window, which is from the transmission of sky light. The sky degree of polarization $P_{sky}$ in this case is 0.77. It is obvious that the ocean surface has a depolarization effect [*Kattawar and Adams*, 1989]. The influence of the ocean surface mainly focuses on the local maximum point and the edge of the Snell's window. Higher wind speed leads to a smaller value of the maximum $\langle P\rangle$. Since MSS, which represents the roughness of ocean surface, approximately linearly increases with $U_{10}$, it can be concluded that the rougher the ocean surface the less in-water light is polarized. The position of the maximum $\langle P\rangle$ varies slightly at different depths. Figures 9a and 9b show the polar angle and azimuthal angle, respectively, of the maximum mean value of the degree of polarization at four depths. It is seen that the surface roughness of the ocean has little influence on the positions of the maximum mean value of degree of polarization. At the depth of $z = -0.3$ m, the polar angle $\theta_{p_{\max}} \approx 41.4°$ and the azimuthal angle $\phi_{p_{\max}} \approx 103.2°$ and 256.7°. At the depth of $z = -2.2$ m, the polar angle $\theta_{p_{\max}} \approx 41.8°$ and the azimuthal angle $\phi_{p_{\max}} \approx 110.4°$ and 249.5°. At the depth of $z = -4.8$ m, the polar angle $\theta_{p_{\max}} \approx 37.7°$ and the azimuthal angle $\phi_{p_{\max}} \approx 125.0°$ and 234.9°. At the depth of $z = -7.5$ m, the polar angle $\theta_{p_{\max}} \approx 36.6°$ and the azimuthal angle $\phi_{p_{\max}} \approx 134.7°$ and 225.2°. We can see that the polar angle of the position of maximum degree of polarization slightly depends on the ocean surface roughness but clearly varies with the depth; the azimuth angle of the position of maximum degree of polarization is not the function of the ocean surface roughness at all and but is the function of the depth.

[35] Before systematically studying the surface roughness effects on the in-water polarization, it is necessary to compare the effects of Cox-Munk surface slope model and ECKV dynamic ocean wave model on the mean value of the in-water polarized light fields. Figure 10a shows the depth dependence of the ratio of maximum mean degree of polarization to sky polarization $\langle P\rangle_{\max}/P_{sky}$ with two wind speeds ($U_{10} = 3$ and 21 m s$^{-1}$) as a comparison between Cox-Munk surface slope model and ECKV dynamic ocean wave model. It is seen that these two models reach the same results in terms of the maximum mean value of the degree of polarization within the Snell's window. The reason to use the dynamic wave model instead of Cox-Munk statistical model is to study the higher-order statistical characteristics (e.g., variance) of the underwater polarized light fields and also to take into consideration the effects of nonlinearity of ocean waves in the study. Figure 10b demonstrates the linear dependence of the ratio $\langle P\rangle_{\max}/P_{sky}$ on the MSS of the ocean surface waves. The fitting lines give different slopes for different depths. The dependence of $\langle P\rangle_{\max}/P_{sky}$ on MSS is weaker at deeper locations, indicating that the effect of ocean waves on polarization diminishes with detector depth.

[36] The probability density function of normalized degree of polarization $P/\langle P\rangle$ is obtained via the 200 realizations of the simulated degree of polarization for each direction. Our interest is in the point with the maximum $\langle P\rangle$ and in two neutral points at the principal plane. The probability density function of these three points are shown in Figure 11. *You et al.* [2010] demonstrated theoretically and experimentally that the probability density function of downwelling irradiance is not symmetric. Unlike the irradiance, we found the probability density function of degree of polarization for certain directions has Gaussian-like shape, but with different width for the three points. From Figures 11a and 11b, it can be seen that $P/\langle P\rangle$ has the largest variance at the Babinet point and the smallest variance at the location with the maximum $\langle P\rangle$. The wind speed used in Figure 11 is $U_{10} = 11$ m s$^{-1}$. Figure 12 shows the dependence of the variance of $P/\langle P\rangle$ on the wind speed $U_{10}$ at several depths. It shows that the variability of $P/\langle P\rangle$ linearly increases with ocean surface roughness, but with different rates at different depths. The variance at smaller depths increases more with the wind speed. In other words, variability of $P/\langle P\rangle$ at shallower depths is more affected by the surface roughness.

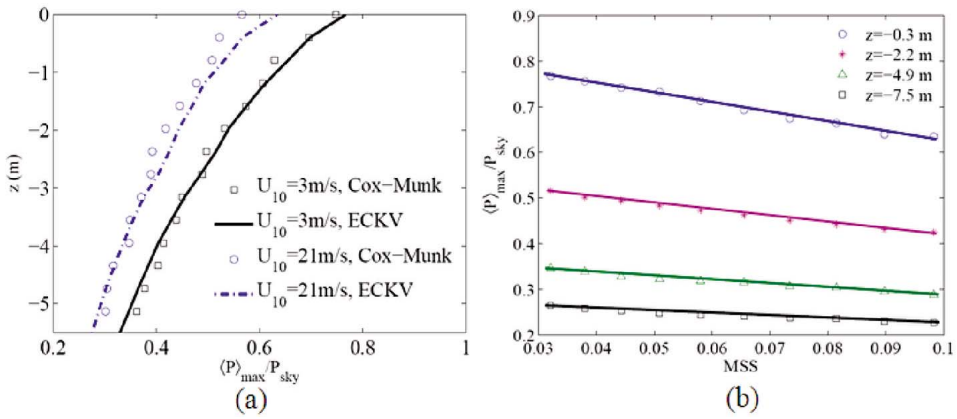


**Figure 10.** Dependence of ratio $\langle P\rangle_{\max}/P_{sky}$ within the Snell's window on the MSS of the ocean surface. (a) Comparing $\langle P\rangle_{\max}/P_{sky}$ under the dynamic ECKV ocean surface with that under the Cox-Munk ocean surface for different ocean depths in the cases of two wind speeds ($U_{10}$ = 3 and 21 m s$^{-1}$). Agreement between the dynamic ECKV surface and the Cox-Munk surface is shown. (b) Dependence of $\langle P\rangle_{\max}/P_{sky}$ on the MSS of the ocean surface at different depths ($z$ = −0.3, −2.2, −4.9, and −7.5 m). The solar incidence is ($\theta_{sun}$ = 65°, $\phi_{sun}$ = 0°); the light wavelength $\lambda$ = 532 nm; IOPs are obtained from the SBC experiment listed in Table 2. The total beam attenuation coefficient is $c$ = 0.610 m$^{-1}$ and total single scattering albedo is $\omega$ = 0.873.

[37] Different wavelengths of light in water demonstrate very different reactions to the ocean surface as well as water turbidity. We examined three wavelengths, $\lambda$ = 443, 532, and 670 nm. It is noticed that the refractive index of water for these wavelengths are 1.341, 1.336, and 1.332, respectively. From Table 2, we see that the biggest attenuation coefficient is at 443 nm and the biggest single scattering albedo is at 532 nm. The effects of ocean surface waves and water turbidity on the degree of polarization inside and outside the Snell's window can be understood from Figure 13. Figure 13 demonstrates the mean value of the degree of polarization $\langle P\rangle$ on the principal plane for the three wavelengths described above. The ocean surface wave condition is $U_{10}$ = 11 m s$^{-1}$. At a very shallow depth (Figure 13a), $z$ = −0.3 m, the maximum of the degree of polarization inside the Snell's window are the same for the three wavelengths due to the fact that at these shallow depths the polarization pattern is dominated by the downwelling skylight polarization pattern. The effect of the surface is to depolarize the pattern, either through the mixing of different directions in the skylight because of surface wave slope variations, or because of the form of the transmission Mueller matrix [*Kattawar and Adams*, 1989]. Outside the Snell's window, the degree of polarization is smallest at $\lambda$ = 532 nm. This is caused by the depolarization effect of scattering. The higher the single scattering albedo, the smaller the degree of polarization. The same mechanism works at a larger depth (Figure 13b). Both inside and outside the Snell's window,

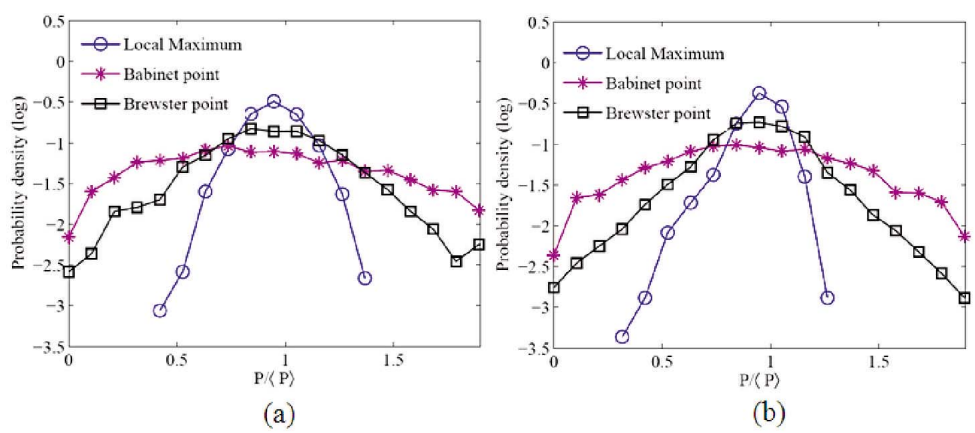


**Figure 11.** Probability density function of the degree of polarization at the position of the maximum time-averaged $\langle P\rangle_{\max}$ within the Snell's window $\theta \approx 18°$ and two positions of the neutral points for flat ocean surface on the principal plane under wind-driven ocean surfaces with wind speed ($U_{10}$ = 11 m s$^{-1}$). Receiver placed at the depths (a) $z$ = − 0.3 and (b) $z$ = −7.5 m. The solar incidence is $\theta_{sun}$ = 65°, $\phi_{sun}$ = 0°; the light wavelength $\lambda$ = 532 nm; IOPs are obtained from the SBC experiment listed in Table 2. The total beam attenuation coefficient is $c$ = 0.610 m$^{-1}$ and total single scattering albedo is $\omega$ = 0.873.

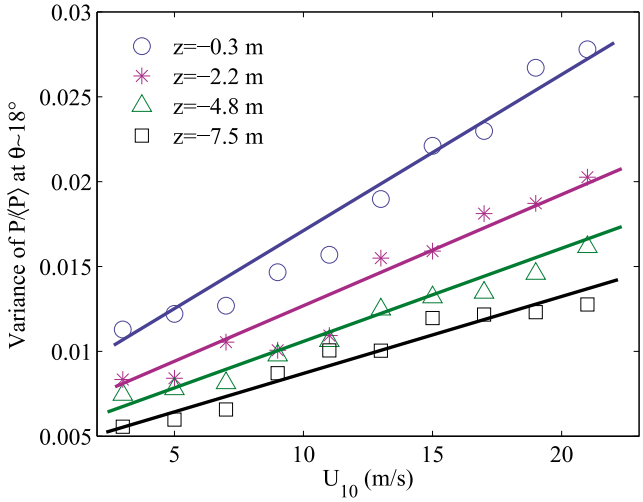


**Figure 12.** Variance of the normalized degree of polarization $P/\langle P\rangle$ at the angular position of local maximum degree of polarization on the principal plane within the Snell's window $\theta \approx 18°$ as a function of wind speed $U_{10}$. Receivers are placed at four depths ($z = -0.3$, $-2.2$, $-4.8$, and $-7.5$ m). The solar incidence is ($\theta_{sun} = 65°$, $\phi_{sun} = 0°$); the light wavelength $\lambda = 532$ nm; IOPs are obtained from the SBC experiment listed in Table 2. The total beam attenuation coefficient is $c = 0.610$ m$^{-1}$ and total single scattering albedo is $\omega = 0.873$.

the major factor affecting the degree of polarization is the scattering. Therefore, light with the smallest single scattering albedo, $\lambda = 670$ nm, has the biggest mean value of the degree of polarization. Figure 13c shows the depth dependence of the ratio of the local maximum mean value of the degree of polarization in water to sky polarization, $\langle P\rangle_{\max}/P_{sky}$. It is obvious that this ratio decreases with depth and light with $\lambda = 670$ nm has the biggest ratio and decreases less with depth. The reason that $\lambda = 443$ nm has a slightly smaller value of this ratio than $\lambda = 532$ nm is that the attenuation coefficient is largest at 443 nm. At the same physical depth, the optical depth of $\lambda = 443$ nm is larger. Therefore, the depolarization effect is stronger for $\lambda = 443$ nm than that for $\lambda = 532$ nm.

### 3.3. Effects of Nonlinearity of Ocean Waves

[38] To understand the effect of wave nonlinearity on the in-water polarization, we consider linear waves and nonlinear waves evolving from the same initial wavefield. For simplicity, a narrow banded JONSWAP [*Hasselmann et al.*, 1973] spectrum is used to generate the two linear waves fields with the MSS of around 0.03 and 0.04. The parameters of JONSWAP spectrum used are $\alpha = 0.023$ and 0.031 for linear waves with MSS equal to 0.03 and 0.04, respectively; $\gamma = 3.3$, $\sigma_1 = 0.07$ and $\sigma_2 = 0.09$. The dominant wavelength of the waves is 0.56 m and the cutoff wave number is 240 m$^{-1}$. The corresponding wind speed $U_{10} = 10$ m s$^{-1}$ with fetch length of 200 m. Using the HOS simulation, a fully nonlinear wavefield is obtained after the initial linear wavefield evolves by 50 dominant periods (≈20 s). MSS of the stable nonlinear wavefield is around 0.04.

[39] Taking steps similar to our polarized radiative transfer investigation, we assume the light wavelength is 532 nm and the solar zenith incidence is ($\theta_{sun} = 65°$, $\phi_{sun} = 0°$). IOPs are from the Santa Barbara Channel experiment. Figure 14 compares the effect of linear and nonlinear waves with same MSS and different MSS, respectively, on polarization in terms of $\langle P\rangle_{\max}/P_{sky}$ and variance of $\langle P\rangle$ at the local maximum of $P$ inside the Snell's window, at the position of $\theta \approx 40°$ and $\phi \approx 110°$. It is seen that the ratio $\langle P\rangle_{\max}/P_{sky}$ for the linear and nonlinear waves with the same MSS (≈0.04) are equal to each other at arbitrary depth. $\langle P\rangle_{\max}/P_{sky}$ induced by the linear waves with MSS = 0.03 is a little larger than that of nonlinear waves (Figure 14a). The main contributions of nonlinear waves are on the variance of the polarized fields. The variance of $P/\langle P\rangle$ at the local maximum point with nonlinear waves is larger than the variances of linear waves with the same and smaller MSS (Figure 14b). This is likely due to the fact that the high-frequency components of ocean wavefields are critical to the variance of $P/\langle P\rangle$ and the nonlinear interaction of wave modes increases the high-frequency components compared with linear waves even with the same MSS. Therefore, it can be expected that in

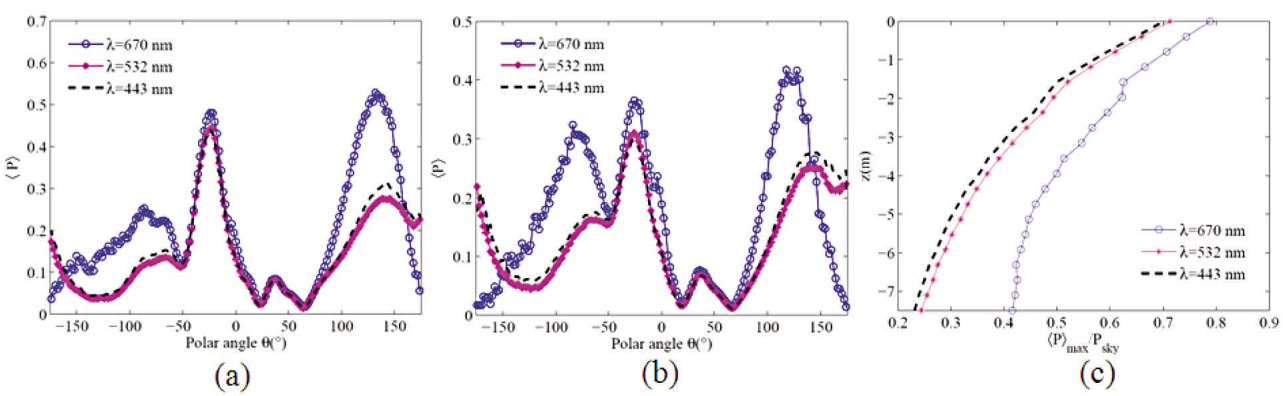


**Figure 13.** Time-averaged degree of polarization $\langle P\rangle$ on the principal plane for light with three different wavelengths ($\lambda = 443$, 532, and 670 nm) under dynamic ECKV ocean surface with $U_{10} = 11$ m s$^{-1}$ for solar zenith incidence ($\theta_{sun} = 65°$, $\phi_{sun} = 0°$). Receiver placed at the depths (a) $z = -0.3$ and (b) $z = -2.2$ m. (c) $\langle P\rangle_{\max}/P_{sky}$ on the principal plane inside the Snell's window as a function of detector depths. The solar incidence is ($\theta_{sun} = 65°$, $\phi_{sun} = 0°$); IOPs are obtained from the SBC experiment listed in Table 2.

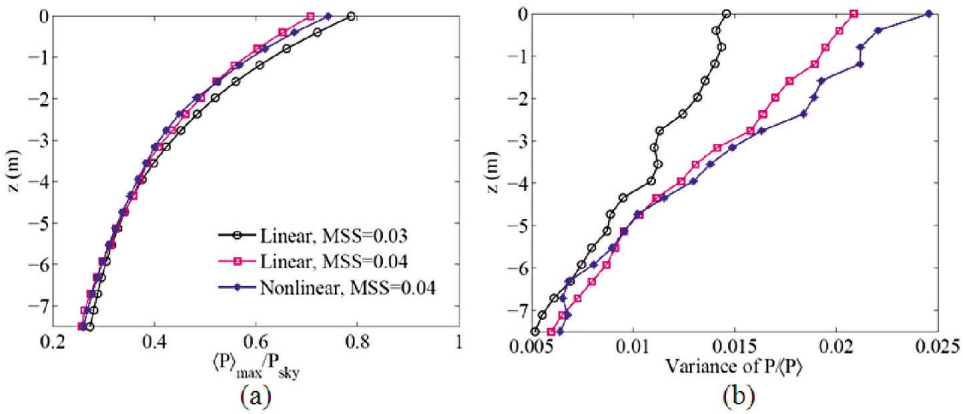


**Figure 14.** Effects of the nonlinearity of ocean waves on the mean value and the variance of the degree of polarization below the ocean surface. The effect of the nonlinear wave with MSS ≈ 0.04 is compared to that of one linear wave with the same MSS (0.04) and one linear wave with relatively smaller MSS (0.03). The solar incidence and IOPs are the same as Figure 8. The interested direction to investigate the degree of polarization is $\theta \approx 40°$ and $\phi \approx 110°$ where a maximum mean degree of polarization within the Snell's window is observed. (a) Depth dependence of the ratios $\langle P \rangle_{\max}/P_{sky}$ and (b) $P/\langle P \rangle$. The solar incidence is ($\theta_{sun} = 65°$, $\phi_{sun} = 0°$); the light wavelength $\lambda = 532$ nm; IOPs are obtained from the SBC experiment listed in Table 2. The total beam attenuation coefficient is $c = 0.610\ \mathrm{m}^{-1}$ and total single scattering albedo is $\omega = 0.873$.

the case of rougher sea surfaces where nonlinearity becomes more dominant, the variance of the in-water polarization is larger than the previous calculations based on a linear wave assumption. In practice, a reasonable correction can be made for fully evolved wave cases.

## 4. Conclusions

[40] In this study, we have studied the in-water polarization patterns and variability properties by means of numerical simulations with comparison to field experiments. A three-dimensional Monte Carlo vector radiative transfer programme has been developed and validated to predict the polarized light propagation in the coupled atmosphere–ocean system with dynamic air-sea boundaries. The program was fully parallelized to achieve quick convergence. High angular resolution of 2° × 2° and small receiver size 5 cm are achieved in the simulation to mimic the experimental instrument performance. Statistical analysis is performed using up to 200 realizations for each case. Field measurements of both sky and in-water Stokes vector components were taken in Santa Barbara Channel in September 2008 and in Hawaii in September 2009 using a DPOL instrument. The MC program was validated from the model-to-data comparison based on those experiments.

[41] We have extensively investigated the influences of the dynamic ocean surface waves on in-water degree of polarization inside the Snell's window. We found that the pattern of the degree of polarization is symmetric about the principal plane. The pattern next to the ocean surface is similar to that of the sky polarization but is confined within the Snell's window for large solar incidence. The maximum degree of polarization occurs at the direction refracted from the 90° contour in air to solar incidence but outside the principal plane. Both polar angle and azimuthal angle of the position of maximum transmitting degree of polarization are the functions of the detector depth, but only polar angle slightly depends on the wind speed at deeper depths. As the MSS of the surface increases, the maximum value of the degree of polarization drops, but its variability increases.

[42] Nonlinearity of ocean surface waves has been examined to determine its effect on the pattern and variability of the degree of polarization. We found that the wave nonlinearity plays a minor role in the formation of the degree of polarization pattern, but it makes an appreciable difference in increasing the variance of it.

[43] With the increasing understanding of the relation between ocean surface waves and the in-water polarization static and fluctuating characteristics, one can expect potential applications in many areas, such as retrieving ocean surface conditions using in-water polarimeter measurements and understanding the orientation mechanism of some marine animals.

[44] **Acknowledgments.** This study was supported by the Office of Naval Research through the RaDyO project. The computing resources were provided by the U.S. Department of Defense High-Performance Computing Modernization Program (HPCMP).

## References

Adams, J. T., and D. J. Gray (2011), Neutral points in an atmosphere–ocean system. Part 2. Downwelling light field, *Appl. Opt.*, *50*, 335–345.

Apel, J. R. (1994), An improved model of the ocean surface wave vector spectrum and its effects on radar backscatter, *J. Geophys. Res.*, *99*, 16,269–16,291.

Beardsley, G. F., Jr. (1968), Mueller scattering matrix of sea water, *J. Opt. Soc. Am.*, *58*, 52–57.

Bhandari, P., K. J. Voss, L. Logan, and M. Twardowski (2011a), The variation of the polarized downwelling radiance distribution with depth in the coastal and clear ocean, *J. Geophys. Res.*, *116*, C00H10, doi:10.1029/2011JC007320.

Bhandari, P., K. J. Voss, and L. Logan (2011b), An instrument to measure the downwelling polarized radiance distribution in the ocean, *Opt. Express*, *19*, 17,609–17,629.

Bjerkaas, A. W., and F. W. Riedel (1979), Proposed model for the elvation spectrum of a wind-roughened sea surface, Tech. Rep. APL-TG-1328-I-31, Appl. Phys. Lab., Johns Hopkins Univ., Laurel, Md.

Chandrasekhar, S. (1950), *Radiative Transfer*, Dover, New York.

Chandrasekhar, S., and D. Elbert (1954), The illumination and polarization of the sunlight sky on Rayleigh scattering, *Trans. Am. Philos. Soc.*, *44*, 643–728.

Cox, C., and W. Munk (1954), Statistics of the sea surface derived from Sun glitter, *J. Mar. Res.*, *13*, 198–227.

Dickey, T. D., G. W. Kattawar, and K. J. Voss (2011), Shedding new light on light in the ocean, *Phys. Today*, *64*, 44–49.

Dommermuth, D. G., and D. K. P. Yue (1987), A high-order spectral method for the study of nonlinear gravity waves, *J. Fluid Mech.*, *184*, 267–288.

Donelan, M. A., and W. J. P. Pierson (1987), Radar scattering and equilibrium ranges in wind-generated waves with application to scatterometry, *J. Geophys. Res.*, *92*, 4971–5029.

Elfouhaily, T., B. Chapron, K. Katsaros, and D. Vandemark (1997), A unified directional spectrum for long and short wind-driven waves, *J. Geophys. Res.*, *102*, 15,781–15,796.

Hasselmann, K., et al. (1973), Measurements of wind-wave growth and swell decay during the Joint North Sea Wave Project (JONSWAP), *Dtsch. Hydrogr. Z.*, *12*, 1–95.

Horváth, G., and D. Varjú (1997), Underwater refraction–polarization patterns of skylight perceived by aquatic animals through Snell's window of the flat water surface, *Vision Res.*, *35*, 1651–1666.

Ivanoff, A., and T. H. Waterman (1958), Factors, mainly depth and wavelength, affecting the degree of underwater light polarization, *J. Mar. Res.*, *15*, 283–307.

Kadyshevich, Y. A., Y. S. Lyubovtseva, and I. N. Plakhina (1971), Measurement of matrices for light scattered by sea water, *Izv. Acad. Sci. USSR Atmos. Oceanic Phys., Engl. Transl.*, *7*, 367–371.

Kattawar, G. W., and C. N. Adams (1989), Stokes vector calculations of the submarine light field in an atmosphere–ocean with scattering according to a Rayleigh phase matrix: Effect of interface refractive index on radiance and polarization, *Limnol. Oceanogr.*, *34*, 1453–1472.

Kattawar, G. W., G. N. Plass, and J. A. Guinn Jr. (1973), Monte Carlo calculations of the polarization in the Earth's atmosphere–ocean system, *J. Phys. Oceanogr.*, *3*, 353–372.

Liu, Y., and K. J. Voss (1997), Polarized radiance distribution measurement of skylight: Part II. Experiment and data, *Appl. Opt.*, *36*, 8753–8764.

Petzold, T. J. (1972), Volume scattering functions for selected ocean water, *SIO Ref.*, *72–78* 79 pp., Scripps Inst. Oceanogr., San Diego, Calif.

Pope, R. M., and E. S. Fry (1997), Absorption spectrum (380–700 nm) of pure water: Part II. Integrating cavity measurements, *Appl. Opt.*, *36*, 8710–8723.

Sabbah, S., and N. Shashar (2006), Underwater light polarization and radiance fluctuations induced by surface waves, *Appl. Opt.*, *45*, 4726–4739.

Sabbah, S., and N. Shashar (2007), Light polarization under water near sunrise, *J. Opt. Soc. Am. A*, *24*, 2049–2056.

Sabbah, S., A. Barta, J. Gal, G. Horvath, and N. Shashar (2006), Experimental and theoretical study of skylight polarization transmitted through Snell's window of a flat water surface, *J. Opt. Soc. Am. A*, *23*, 1978–1988.

Smith, R. C., and K. S. Baker (1981), Optical properties of the clearest natural waters (200–800 nm), *Appl. Opt.*, *20*, 177–184.

Tynes, H. H., G. W. Kattawar, E. P. Zege, L. L. Katsev, A. S. Prikhach, and L. I. Chikovskaya (2001), Monte Carlo and multicomponent approximation methods for vector radaitive transfer by use of effective Mueller matrix calculations, *Appl. Opt.*, *40*, 400–412.

Voss, K. J., and E. S. Fry (1984), Measurement of the Mueller matrix for ocean water, *Appl. Opt.*, *23*, 4427–4439.

Voss, K. J., and Y. Liu (1997), Polarized radiance distribution measurements of skylight: Part I. System description and characterization, *Appl. Opt.*, *36*, 6083–6094.

Voss, K. J., P. Bhandari, and L. Logan (2008), A new spectral polarized radiance distribution camera system: DPOL, paper presented at Ocean Optics XIX, Oceanogr. Soc., Barga, Italy.

Waterman, T. H., and W. E. Westell (1956), Quantitative effect of the Sun's position on submarine light polarization, *J. Mar. Res.*, *15*, 149–169.

Wehner, R. (2001), Polarization vision—A uniform sensory capacity?, *Vision Res.*, *35*, 2589–2596.

West, B. J., K. A. Brueckner, R. S. Janda, M. Milder, and R. L. Milton (1987), A new numerical method for surface hydrodynamics, *J. Geophys. Res.*, *889*, 11,803–11,824.

You, Y., D. Stramski, M. Darecki, and G. W. Kattawar (2010), Modeling of wave-induced irradiance fluctuations at near-surface depths in the ocean: A comparison with measurements, *Appl. Opt.*, *49*, 1041–1053.

L. Shen, Department of Civil Engineering, Johns Hopkins University, 3400 N. Charles St., Baltimore, MD 21218, USA. (lianshen@jhu.edu)

K. J. Voss, Atmospheric and Oceanic Optics Laboratory, Department of Physics, University of Miami, 1320 Campo Sano Dr., Coral Gables, FL 33146, USA.

Z. Xu and D. K. P. Yue, Department of Mechanical Engineering, Massachusetts Institute of Technology, 77 Massachusetts Ave., Cambridge, MA 02139–4307, USA. (xuzao@mit.edu; yue@mit.edu)